PCCP

In-situ vibrational spectroscopy of adsorbed nitrogen in porous carbon materials

SCHOLARONE™
Manuscripts

In-situ vibrational spectroscopy of adsorbed nitrogen in porous carbon materials

Paramita Ray[±, β], Enshi Xu[€, β], Vincent H. Crespi[±, €, ¥, β], John V. Badding[±, €, ¥, β], Angela D. Lueking[£, σ, λ,*]

Departments of [±]Chemistry, [€]Physics, [¥]Materials Science and Engineering, [£]Energy & Mineral Engineering, [β]Material Research Institute
[σ]Chemical Engineering, [λ]EMS Energy Institute, The Pennsylvania State University, University Park, PA,16802, USA

*Corresponding Author: Email:adl11@psu.edu Tel. 814-863-6256

ABSTRACT: This study uses *in-situ* vibrational spectroscopy to probe nitrogen adsorption to porous carbon materials, including single-wall carbon nanotubes and Maxsorb super-activated carbon, demonstrating how the nitrogen Raman stretch mode is perturbed by adsorption. In all porous carbon samples upon N_2 physisorption in the mesopore filling regime, the N_2 Raman mode downshifts by ~2 cm^{-1}, a downshift comparable to liquid N_2. The relative intensity of this mode increases as pressure is increased to saturation, and trends in the relative intensity parallel the volumetric gas adsorption isotherm. This mode with ~2 cm^{-1} downshift is thus attributed to perturbations arising due to N_2-N_2 interactions in a condensed film. The mode is also observed for the activated carbon at 298 K, and the relative intensity once again parallels the gas adsorption isotherm. For select samples, a mode with a stronger downshift (>4 cm^{-1}) is observed, and the stronger downshift is attributed to stronger N_2-carbon surface interactions. Simulations for a N_2 surface film support peak assignments. These results suggest that N_2 vibrational spectroscopy could provide an indication of the presence or absence of porosity for very small samples.

KEYWORDS: Adsorption, Spectroscopy, Nitrogen, Carbon nanotubes, activated carbon

INTRODUCTION

The pore size distribution of a porous material dictates its performance in gas separation, storage, and catalytic applications. Generally, methods for pore size analysis fall into two categories: those that directly characterize the pore structure (typically through interaction with probe particles, such as X-ray photons,[1-3] neutrons, electrons,[4] or positrons[5-7]) and those that indirectly fit excess experimental gas adsorption data to a thermodynamic model. The direct methods tend to either be limited to highly localized regions (e.g. transmission electron microscopy) or require access to specialized facilities (e.g. positron annihilation spectroscopy and small angle X-ray scattering). Although experimental gas adsorption probes are readily available, they provide an indirect probe of *excess* adsorption, i.e. measurements are made relative to a non-adsorbing control. Furthermore, determination of pore size from gas adsorption isotherms requires a number of assumptions, based either on classical thermodynamics (e.g., Horvath-Kawazoe[8]), a fitting procedure to match the distribution to that of a series of simulated isotherms for idealized pore structures (e.g. non-local density functional theory (NLDFT)[9]) , or fit to models based on a uniform adsorption potential (Polayni[10] and Dubinin[11]). One can envision several cases wherein either the model assumptions or the assumed pore structure are inconsistent with the sample structure, in particular for novel materials in which pore geometry is unknown or complex. In some case, insufficient sample quantity may provide an additional hurdle, as we faced in our recent synthesis of polymerized triptycene in a diamond anvil cell.[12]

In-situ spectroscopy may provide an alternative to traditional gas adsorption measurements: it is both widely available and provides a probe of total (rather than excess) adsorption. As it directly probes the perturbation of the electronic environment upon adsorption, it has the potential to be supplemented with *ab initio* calculations to understand trends, alleviating the need for complex (or highly simplified) adsorption models. In this paper, our specific goal is to explore how pore structure and adsorption potential (i.e. temperature and pressure) affect the vibrational spectra of nitrogen adsorbed to porous carbon materials. In brief, the vibrational mode of the N_2 molecule (at ~2330cm^{-1}) is Raman active, but due to its symmetry, is IR-active only upon adsorption to a surface.[13] Previously, Eklund *et al.* showed how H_2 and D_2 vibrations were perturbed by a few-wavenumbers upon physical adsorption to single-walled carbon nanotubes (SWNT) at 85 K.[14] To the best of our

knowledge, this is the only paper that probes how the Raman spectra of a diatomic molecule is perturbed upon physical adsorption. The Eklund et al. paper does not study how the perturbation induced by physical adsorption is sensitive to pore structure and adsorption potential. To establish these relationships, we have chosen nitrogen as the probe molecule, as it is the most widely-used adsorbate in conventional gas adsorption measurements. Trends for nitrogen adsorption in carbon pores are well established,[15-16] and we have chosen single-walled carbon nanotubes (SWNT) and activated carbon (AC) as experimental analogs of idealized cylindrical and slit pores, respectively. Complementary *ab initio* modeling and traditional volumetric measurements are used to substantiate the spectroscopic trends.

EXPERIMENTAL

SWNT were purchased from (a) Sigma Aldrich, (b) Thomas Sawn, and (c) Cheaptubes. As reported by the manufacturers, all SWNT samples had open tubes with diameters of (a) 0.7–0.9 nm, (b) 1.2 nm (average diameter), and (c) 1–2 nm. Prior to receipt, various pretreatments such as sonication were used by the manufacturers to purify the nanotubes. Maxsorb AC was provided to us by the National Renewable Energy, synthesized by Tokyo Zairyo Co. Laboratory via KOH activation at ~800 °C. A small film of highly ordered pyrolitic graphite (HOPG) was used as a Raman standard.

A Micromeritics ASAP 2020 volumetric adsorption unit collected nitrogen adsorption isotherms at 77 K up to the saturation pressure (P_0). Both SWNT and AC samples were pre-treated at 120°C for 12 hours under vacuum prior to the volumetric adsorption measurement. Adsorption isotherms were fit to the standard NLDFT model[9] and the Maxsorb was also fit to the 2D-NLDFT heterogeneous surface[17-18] model to calculate the PSD, assuming carbon cylindrical pores for the SWNT, and carbon slit pores for the AC. The BET surface area was calculated within a relative pressure range (P/P_0) of 0.05 to 0.3 for SWNT and 0.004 to 0.3 for AC. To compare adsorption of N_2 at 77 K and 298 K, which represent sub-critical and super-critical conditions, the reduced chemical potential was used (i.e. normalizing temperature and pressure by the critical values), as developed elsewhere [19-21].

In situ Raman spectra were collected with a Renishaw *Invia* spectrometer using 633 nm excitation with a dispersion of 1cm$^-$^{1} per pixel, using a 20✕ objective with a numerical aperture of 0.35. To verify the tube diameters claimed by the manufacturers, low-frequency Raman spectra were collected on a Witec instrument with 514 nm excitation wavelength using an Ar-ion laser with a Optigrate notch filter. Carbon samples were pretreated *ex situ* prior to Raman measurements, as our current set-up does not allow for high vacuum pretreatment. Samples were pressed onto double-sided scotch tape and then placed into a Linkam stage (THMS600PS Pressure System) capable of measurements between 77 and 873 K. Pressure was controlled via the gas regulator, and measured via an electronic gauge with sensitivity of ~0.1psi. The liquid nitrogen cooling system is connected to the stage through a dewar siphon; warm recycled nitrogen gas was blown across the stage window to avoid condensation and fogging. The 1.3 mm diameter aperture was fitted with quartz windows. Raman spectra were fitted by Lorentzian curves with cubic background subtraction. Spectral peak widths were comparable to instrument resolution and were typically less than 2 CCD pixels, so no attempt was made to deconvolute the Lorentizan Raman and Gaussian instrument components. TEM images were collected on a LaB_6 emitter TEM JEOL microscope after sonicating the SWNT samples in ethanol for 30 minutes and drop casting onto a Cu grid. Intensity ratio is considered rather than area ratio as Raman scattering is sensitive to sample thickness. Direct comparisons between intensity ratio were limited to samples of comparable sample thickness (e.g. AC was not directly compared to SWNT), and averages from several spots were used.

To support assignment of the Raman modes, we simulated monolayer and multilayer adsorption of N_2 molecules onto graphene. Both herringbone and pinwheel structures were used as the initial configuration for the monolayer calculations. The herringbone configuration with AA stacking was used for either two or eight multilayer structures. All internal atomic coordinates were fully relaxed, but the lattice was fixed at the ideal graphene value. Adsorption energy, or binding energy, was calculated as $E_b = \frac{1}{n}\left(E_{graphene} + nE_{isolated\ N_2} - E_{N_2\ on\ graphene}\right)$, where *n* is the number of molecules adsorbed onto the graphene substrate; thus a larger positive binding energy means stronger adsorption. The structural relaxations, adsorption energies and vibrational frequencies of adsorbed N_2 were calculated within first-principles density functional theory using the VASP package[22-24]. Exchange-correlation was treated with the PBE generalized gradient approximation and the core potential was treated with projector-augment waves (PAW).[25-28] An energy cutoff of 600 eV and a k-point mesh finer than 0.22 A^{-1} ensure convergence to within 1 meV per atom. van der Waals contributions were described using the method of Tkatchenko and Scheffler[29]. Periodic boundary conditions were employed in all three dimensions. A vacuum region of at least 10 Å was imposed between the top layer of adsorbed N_2 molecules and the nearest graphene periodic image. The vibrational frequencies of the fully relaxed structure were calculated using the frozen phonon method.

RESULTS AND DISCUSSION

TEM images (Figure 1) of the SWNT as well as analysis of the radial breathing modes (reported elsewhere[30]) are consistent with the tube diameter range stated by the manufacturers. The TEM images of the three different SWNT samples indicated

that all are bundled. Residual encapsulated catalyst particles and amorphous materials are obvious in the TEM of the 0.7–0.9 nm SWNT, despite efforts by the manufacturer to remove impurities.

N_2 adsorption at 77K from traditional volumetric adsorption techniques (Figure 2) shows the SWNTs have a type-IV isotherm, indicative of a material with both micro- and mesoporous regions. The mesoporous regions (>2 nm) are likely attributable to a combination of spaces between tube bundles and amorphous regions. No major differences were observed between the adsorption isotherms of different SWNT samples, with only minor differences in the calculated BET surface areas, with a range of 520–640 m^2/g (Figure 2, Table 1). The NLDFT PSD calculation delineated only minor distinctions between samples (Figure 2c, Table 1). Subtle differences can be found in the ~1nm pore region that trend with tube size. The 1–2 nm SWNT has a slightly broader PSD in the 0.5–1.5 nm range than the other SWNT, consistent with the manufacturer-reported tube diameter; the 1.5–3 nm range of pore sizes for this sample was decreased relative to the other SWNT.

The Maxsorb AC N_2 isotherm is indicative of a high surface area (3290 m^2/g) material, with a considerable increase in capacity for N_2 adsorption relative to the SWNT. The cumulative pore volume is over one order of magnitude higher than that of the SWNT (Figure 2b, Table 1), with a bimodal pore distribution of micropores and small mesopores.

Free nitrogen has a Raman-active symmetric stretch mode at ~2330 cm^{-1} (Figure 3), which we will denote as $N_2(I)$. For all carbon materials examined, across all conditions investigated, no appreciable frequency shifts or broadening were seen in the free $N_2(I)$ mode. The first N_2 adsorption conditions considered were 79 K and 0.48 bar. *In situ* Raman of N_2 at these conditions in the vicinity of non-porous HOPG is virtually indistinguishable from that of free N_2. In contrast, physical adsorption of N_2 to all porous carbon materials gives rise to a secondary vibrational mode, $N_2(II)$, that is downshifted by 1–2 cm^{-1} relative to $N_2(I)$ (Figure 3, Table 2). The $N_2(II)$ frequency is similar in all carbon samples examined, ranging only from 2328.7 to 2329.4 cm^{-1} for the SWNT and sitting at 2328.7 cm^{-1} for the AC. The $N_2(II)$ mode is thus fairly independent of the detailed pore structure of the material. The $N_2(II)$ frequency shift is similar to those expected for condensed N_2, whose modes have been previously measured to be 2328.0 cm^{-1} and 2326 cm^{-1} for liquid[31] and solid[32] nitrogen, respectively. The conditions of 79 K and 0.48 bar correspond to adsorption in mesopores (dotted line, inset, Figure 2), as the pressure is well beyond the monolayer plateau (P/Po <0.1). The $N_2(II)$ mode is thus attributed to a condensed multilayer film. The downshift of the nitrogen peak upon adsorption is indicative of bond softening that arises due to nearest neighbor N_2-N_2 interactions in the adsorbed film.

The 1–2 nm diameter SWNT and the Maxsorb AC also have a tertiary $N_2(III)$ mode at 2326.8 cm^{-1} and 2325.6 cm^{-1}, respectively. The stronger downshift of the $N_2(III)$ mode indicates greater bond softening. We attribute this mode to adsorption into micropores which accommodate overlap of the surface potentials, leading to increased N_2-carbon interaction. The reason for the lack of a pronounced $N_2(III)$ mode in the other SWNT samples is not fully clear, but could be associated with distinctions made above for the PSD of the 1–2 nm SWNTs (Figure 2c). In this critical pore size regime, a slight increase in diameter will allow for faster penetration and less susceptibility to pore blockage resulting from transfer to the Linkham   stage   after   *ex*   *situ*   pretreatment.

N_2 physisorption also leads to concomitant shifts in the carbon vibrational modes, with the 1.2 nm SWNT shown as an example. In the absence of N_2 physical adsorption, the 1.2 SWNT has the expected characteristic vibrational modes of a carbonaceous material, including the G^- (graphitic) peak, D (defect) peak, and G^+ peak (sp^2 carbon-carbon stretching), at 1551.7 cm^{-1}, 1323.4 cm^{-1}, and 1591.8 cm^{-1} respectively (Figure 4). N_2 physisorption (at 79 K, 0.48 bar) shifts these features by +2.2cm^{-1} (G^-), +2cm^{-1} (G^+), and +3.5cm^{-1} (D). Previously, shifts in the carbon vibrational modes have been attributed to weak charge transfer in the system of I_2 absorbed in nanotubes, accompanied by a resistivity study [33]. However, the wide HOMO-LUMO gap of nitrogen molecule would prevent explicit charge transfer, and the nature of the carbon mode shift awaits further study.

The 0.7–0.9 nm SWNT sample was selected for pressure-dependent measurements, as it had the smallest reported diameter distribution. At 79 K, pressure was increased in increments of 0.1–0.3 bar to a final P/P_0 of 0.96. All pressures studied were within the multilayer mesoporous filling regime. As the mesopores fill with increasing pressure, the intensity of the $N_2(II)$ peak (relative to the $N_2(I)$ peak) increases (Figure 5a). Above 0.48 bar, the position and width of the $N_2(II)$ mode approach constant values (Figure 5b,c), suggesting a uniform nearest-neighbor environment in an adsorbed multilayer film. The $N_2(II)/N_2(I)$ intensity ratio is compared to the volumetric N_2 adsorption isotherm in (Figure 5d) for consistency with subsequent comparisons where greater pressure resolution is possible.

The highly microporous AC was selected for investigation at 298 K. An increased temperature allows for greater sensitivity to pressure increments in the microporous regime, but greatly decreases adsorption. At 298 K, the relative intensity of the $N_2(II)$ mode parallels the adsorption isotherm (Figure 6b), when both are converted to reduced chemical potential [20-21] to compensate for temperature differences. There is qualitative agreement in the behavior of the Raman signal with that of the traditional volumetric isotherm.

vdW-DFT calculations of both monolayer and multilayer adsorbed N_2 film on graphene were performed to shed further light on the peak assignments given above. Our vdW-DFT calculations yields a binding energy of 0.13 eV for a single isolated N_2 molecule adsorbed on graphene, consistent with a compilation of both semi-empirical and experimental data for a single N_2 on graphite, which consistently yield a binding energy of around 0.1 eV.[34] We estimate the uncertainty in the calculated frequency shifts to be ± 2 cm^{-1} due to the complex energy landscape, large number of molecules in the structure, and treatment of relatively weak van der Waals interactions within the framework of first-principle density functional theory. Nevertheless, we expect the calculations to provide some insight as to how various configurations may influence vibrational frequency.

First, we explore the binding energy and frequency shift for both herringbone or pinwheel N_2 monolayers on graphene. The herringbone N_2 monolayer has all molecules parallel to graphene, with adjacent N_2 molecules in different in-plane orientations (Figure 7a). The pinwheel configuration has one of the four N_2 molecules in the unit cell oriented perpendicular to the graphene plane (Figure 7d). The vdW-DFT binding energies are calculated to be 0.150 eV and 0.166 eV per N_2 molecule for the herringbone and pinwheel structures, respectively. The calculations predict the pinwheel is slightly energetically preferred, which is inconsistent with prior semi-empirical calculations (using potentials fit to Leonard-Jones and static Coulombic interactions)[35], as well as prior experimental data.[36] The discrepancy is attributed to the vdW-DFT methodology. Relative to the free N_2 vibration, the downshifts for the herringbone and pinwheel structures are <1 cm^{-1} and 1–4 cm^{-1}, respectively. The more pronounced downshift for the pinwheel reflects the inequivalent molecules within the unit cell, with the largest downshift from the molecule perpendicular to the basal plane.

Multiple layers of N_2 molecules in proximity to one graphene plane (inserting a vacuum buffer layer to the next unit cell) were also considered in an attempt to represent adsorption in carbon mesopores. An initial AA herringbone stacking of multiple layers was created and then allowed to relax. In the multilayers, relaxation tended to lead to tilting out of the plane parallel to graphene (Figure 7b-c and Figure 7f). Per N_2 molecule, the vdW-DFT binding energy was 0.151 eV for a bilayer structure and 0.171 for an eight-layer structure. The calculated N_2 stretching frequency is upshifted by 1–4 cm^{-1} in the bilayer structure and downshifted by 2–4 cm^{-1} for the eight-layer structures, with an estimated ± 2 cm^{-1} uncertainty. The unrealistic upshift might be resolved if an overlapping surface potential is imposed by eliminating the vacuum region above the second layer. In the eight-layer structure, molecules that were tilted away from the plan gave rise to the largest shift, as was the case for the monolayer pinwheel structure.

The experimental observations in Table 2 show downshifts from 1.3 to 2.2 cm^{-1} and 4.2 to 5.3 cm^{-1} for N_2(II) and N_2(III) modes, respectively, which are in reasonable overall agreement with the calculations. However, due to the uncertainty in the vdW-DFT calculations, more precise assignment is not possible. However, the small shifts of the monolayer structures (<2 cm^{-1} in both cases) suggest this is not associated with the N_2(III) modes. However, in the calculations there was no overlap in the surface potential of adjacent graphene layers, as a vacuum region is imposed between the topmost N_2 layer and the next graphene layer. Thus, overlap of surface potential via a pore-filling mechanism cannot be ruled out. A subsequent study will explore the role of overlapping surface potential in nanotubes of varying diameter to further explore the N_2(III) mode.

CONCLUSIONS

Physisorption of N_2 in a porous carbon material perturbs the N_2 vibrational spectrum. The effect was particularly pronounced for multi-layer adsorption in the mesoporous filling regime. As N_2 fills the mesopores, the N_2 stretching frequency in the adsorbed film becomes pressure-invariant, as the nearest neighbor environment begins to represent that of a liquid. The integrated relative intensity of the adsorbed film relative to that of free nitrogen parallels the adsorption isotherm collected with traditional volumetric adsorption methods. As Raman scattering is sensitive to sample thickness, the presence of this perturbed N_2 Raman mode provides a qualitative indication of an adsorbed film, and thus an indication of porosity when it occurs below the condensation point of the bulk fluid. In two cases, a highly microporous activated carbon and a SWNT with a broad tube distribution, there was an indication of a stronger perturbation which we potentially attribute to overlapping surface potential. Future studies are directed towards seeking to increase the sensitivity to the microporous regime by achieving finer pressure control at cryogenic conditions.

SUPPORTING INFORMATION

A Supporting Information file includes N_2 Raman data as a function of pressure on 0.7-0.9nm SWNT at 79K (S1), N_2 Raman data as a function of pressure for N_2 adsorbed on Maxsorb-AC at 298K (S2), Raman spectroscopy of SWNT showing the Radial breathing mode at 514nm (S3), and RBM and corresponding SWNT diameter obtained from 514nm Raman spectra(S4).

ACKNOWLEDGMENTS

REFERENCES

1.   Ehrburger-Dolle, F.; Fairen-Jimenez, D.; Berthon-Fabry, S.; Achard, P.; Bley, F.; Carrasco-Marin, F.; Djurado, D.; Moreno-Castilla, C.; Morfin, I. *Carbon* 2005, **43**, 3009.
2.   Jacobsohn, L. G.; Capote, G.; da Costa, M. E. H. M.; Franceschini, D. F.; Freire, F. L. *Diam. Relat. Mater.* 2002, **11,** 1946.
3.   Smorgonskaya, E. A. *Semiconductors* 2003, **37**, 769.
4.   Florea, I.; Ersen, O.; Hirlimann, C.; Roiban, L.; Deneuve, A.; Houlle, M.; Janowska, I.; Nguyen, P.; Pham, C.; Pham-Huu, C. *Nanoscale* 2010, **2**, 2668.
5.   Gidley, D. W.; Peng, H. G.; Vallery, R. S. *Annu. Rev. Mater. Res.* 2006, **36**, 49.
6.   Vallery, R. S.; Liu, M.; Gidley, D. W.; Launey, M. E.; Kruzic, J. J. *Appl. Phys. Lett.* 2007, **91,** 261908.
7.   Bigg, D. M. *Polym. Eng. Sci.* 1996, **36,** 737.
8.   Horvath, G.; Kawazoe, K. *J. Chem. Eng. Jpn* 1983, **16,** 470.
9.   Lastoskie, C.; Gubbins, K. E.; Quirke, N. *J. Phys. Chem.* 1993, **97**, 4786.
10.   Polanyi, M. *Trans. Faraday Soc.* 1932, **28,** 316.
11.   Dubinin, M. M. *Chem. Rev.* 1960, **60**, 235.
12.   Ray, P.; Gray, J. L.; Badding, J. V.; Lueking, A. D. *J. Phys. Chem. B,* 2016, **120,** 11035.
13.   Nijem, N.; Thissen, P.; Yao, Y. P.; Longo, R. C.; Roodenko, K.; Wu, H. H.; Zhao, Y. G.; Cho, K.; Li, J.; Langreth, D. C.; Chabal, Y. J. *J. Am. Chem. Soc.* 2011, **133**, 12849.
14.   Williams, K. A.; Pradhan, B. K.; Eklund, P. C.; Kostov, M. K.; Cole, M. W. *Phys. Rev. Lett.* 2002, **88**, 235-241.
15.   Seaton, N. A.; Walton, J. P. R. B.; Quirke, N. *Carbon* 1989, **27**, 853.
16.   Mikhail, R. S.; Brunauer, S.; Bodor, E. E. *J. Colloid Interf. Sci.* 1968, *26*, 45.
17.   Jagiello, J.; Olivier, J. P. *Adsorption* 2013, **19**, 777.
18.   Jagiello, J.; Olivier, J. P. *Carbon* 2013, **55**, 70.
19.   Quinn, D. F. *Carbon* 2002, **40**, 2767.
20.   Kim, H. Y.; Lueking, A. D.; Gatica, S. M.; Johnson, J. K.; Cole, M. W. *Mol. Phys.* 2008, **106**, 1579.
21.   Sircar, S.; Pramanik, S.; Li, J.; Cole, M. W.; Lueking, A. D. *J. Colloid Interface Science* 2015, **446**, 177.
22.   Kresse, G.; Hafner, J. *Phys. Rev. B* 1994, **49**, 14251.
23.   Kresse, G.; Furthmuller, J. *Comp. Mater. Sci.* 1996, **6**, 15.
24.   Kresse, G.; Furthmuller, J. *Phys. Rev. B* 1996, **54**, 11169.
25.   Blochl, P. E. *Phys. Rev. B* 1994, **50**, 17953.
26.   Kresse, G.; Joubert, D. *Phys. Rev. B* 1999, **59**, 1758.
27.   Perdew, J. P.; Burke, K.; Ernzerhof, M. *Phys. Rev. Lett.* 1996, **77**, 3865.
28.   Perdew, J. P.; Burke, K.; Ernzerhof, M. *Phys. Rev. Lett.* 1997, **78**, 1396.
29.   Kresse, G.; Hafner, J. *Phys. Rev. B* 1993, **47**, 558.
30.   Ray, P.; Badding, J. V.; Lueking, A., PhD Thesis, The Pennsylvania State University, 2016.
31.   Scotto, M. *J. Chem. Phys.* 1968, **49,** 5362.
32.   Anderson, A.; Sun, T. S.; Donkersloot, M. C. A. *Can. J. Phys.* 1970, **48**, 2265.
33.   Rao, A. M.; Eklund, P. C.; Bandow, S.; Thess, A.; Smalley, R. E. *Nature* 1997, **388,** 257.
34.   Vidali, G.; Ihm, G.; Kim, H. Y.; Cole, M. W. *Surf. Sci. Rep.* 1991, **12**, 133.
35.   Roosevelt, S. E.; Bruch, L. W. *Phys. Rev. B* 1990, **41**, 12236.
36.   Diehl, R. D.; Toney, M. F.; Fain, S. C. *Phys. Rev. Lett.* 1982, **48,** 177.

Table 1: BET surface area and calculated porosity parameters

Sample	BET SA (m^2/g)	NLDFT Micropore Surface area (m^2/g)	NLDFT Mesopore surface area (m^2/g)	NLDFT Micropore volume (cc/g)	NLDFT Total pore volume (cc/g)
SWNT 0.7–0.9nm	580	109	181	0.070	1.06
1.2nm	640	111	201	0.074	1.00
1-2nm	520	115	154	0.068	1.09
AC-Maxsorb[a]	3290	1800	501	1.01	1.64

[a]AC calculated with the 2D-NLDFT heterogeneous surface mode.[23-24]

Table 2: Fits of the Raman Spectra of Figure 3 to a Lorentzian with cubic background subtraction.

SWNT[a]	$N_{2(I)}$ Peak position	FWHM-$N_{2(I)}$ (cm^{-1})	$N_{2(II)}$ peak position (cm^{-1})	$\Delta N_{2(II)}$ (cm^{-1}) Relative to HOPG	FWHM-$N_{2(II)}$	$\Delta N_{2(III)}$ (cm^{-1}) Relative to HOPG	FWHM-$N_{2(III)}$	$IN_{2(II)}/IN_{2(I)}$[b]
0.7–0.9nm	2331	1.3	2329.5	−1.3	1.7	-	-	0.51
1.2nm	2330.9	1.6	2328.7	−2.2	2.8	-	-	0.35
1-2nm	2331	0.9	2329.4	−1.5	1.5	−4.2	2.2	0.22
HOPG	2330.9	1.5	-	-	-	-	-	-
AC-Maxsorb	2330.5	1.5	2328.8	−2.1	3.1	−5.3	2.7	0.69 [0.28][b]

[a] Similar data corresponding to Figures 5-6 can be found in the Supporting Information.

[b] Number in brackets is $IN_{2(III)}/IN_{2(I)}$ for AC-Maxsorb. Raman scattering depends on the scattering frequency and is thus dependent upon sample thickness. A direct comparison of intensity ratio for samples of different thickness should be avoided.

FIGURE CAPTIONS

Figure 1. Representative TEM images of SWNT samples with tube diameters of (a) 1.2nm, (b) 1–2nm, and (c) 0.7-0.9 nm.

Figure 2. (a) N_2 adsorption isotherms of the SWNTs and AC at 77K (logarithmic; linear as inset), with calculated surface areas indicated. (b-c) Corresponding NLDFT pore size distributions (in units of cc(STP)/g/Å).

Figure 3. *In situ* N_2 Raman adsorption at 79 K and 0.48 bar on various diameter SWNTs (as indicated), AC, and non-porous highly ordered pyrolytic graphite (HOPG), relative to free N_2. The presence of a secondary N_2(II) perturbation for the SWNT and AC but not HOPG is attributed to the formation of a multilayer adsorbed film associated with mesopore filling. A tertiary N_2(III) mode in also visible in certain cases, as discussed in the main text. The dotted line shows the curve fitting and the solid black lines under each spectra shows the components of the fit.

Figure 4. Carbon Raman modes show a shift in the D and and G peaks as a result of N_2 adsorption at 79 K and 0.48 bar. Data for the 1.2 nm SWNT is shown

Figure 5. (a) *In-situ* Raman spectra of N_2 adsorbed to the SWNT (0.7–0.9nm) at 79 K, as pressure is increased in the mesopore-filling regime. (b) Corresponding shift in peak position (N_2(II)-N_2(I)), (c) FWHM, and (d) relative Raman intensity plotted with the volumetric data. The Raman data in (b)–(d) are determined from Lorentzian fits from averages of multiple Raman spectra at multiple spots of the sample. See also Table S1 of the Supporting Information. In (d), both data sets have been normalized per the maximum value as P→Po.

Figure 6: (a) *In-situ* N_2 Raman spectroscopy of N_2 adsorbed onto Maxsorb AC at room temperature as a function of pressure. (b) The intensity ratio of Raman at 298 K of the N_2(II) to N_2(I) Raman modes parallels the 77K volumetric data. In (b), the y-axis of both data sets is normalized to the value as P→Po.

Figure 7: Relaxed structures for N_2 thin films adsorbed on graphene. (a) Side view of monolayer herringbone. (b) Top view of bi-layer herringbone, the highlighted molecules are in the top layer (c) Side view of bi-layer herringbone. (d) side view and (e) top view of monolayer pinwheel (f, lower left) side view of an eight-layered N_2 thin film relaxed from an initial herringbone configuration.

HIGH RESOLUTION FIGURES UPLOADED AS SEPARATE FILES.
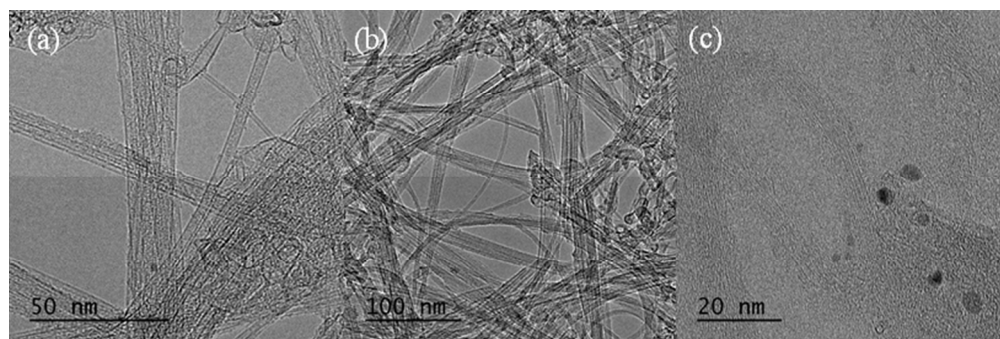
Figure 1: Representative TEM images of SWNT samples with tube diameters of (a) 1.2nm, (b) 1–2nm, and (c) 0.7-0.9 nm.

215x71mm (96 x 96 DPI)
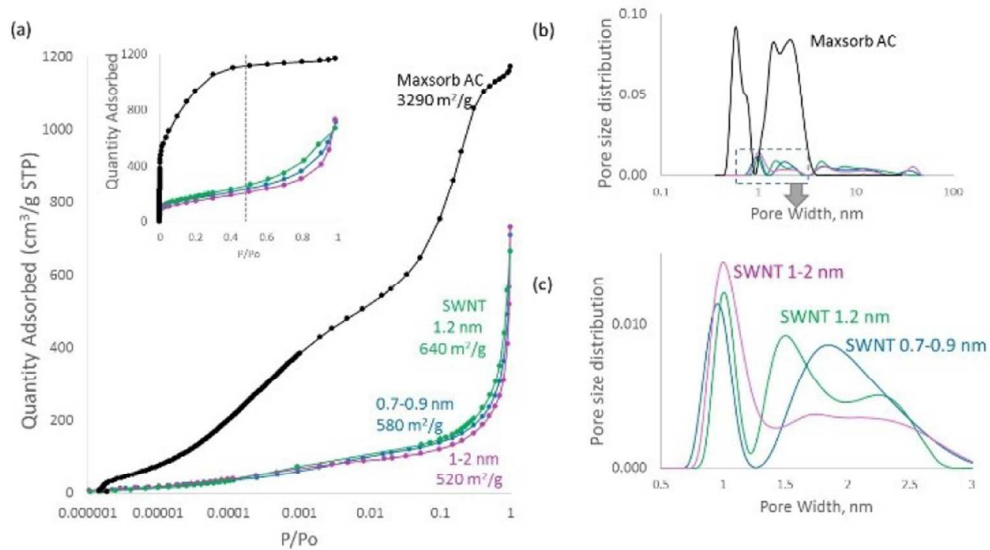
Figure 2: (a) N2 adsorption isotherms of the SWNTs and AC at 77K (logarithmic; linear as inset), with calculated surface areas indicated. (b-c) Corresponding NLDFT pore size distributions (in units of cc(STP)/g/Å).

84x48mm (300 x 300 DPI)
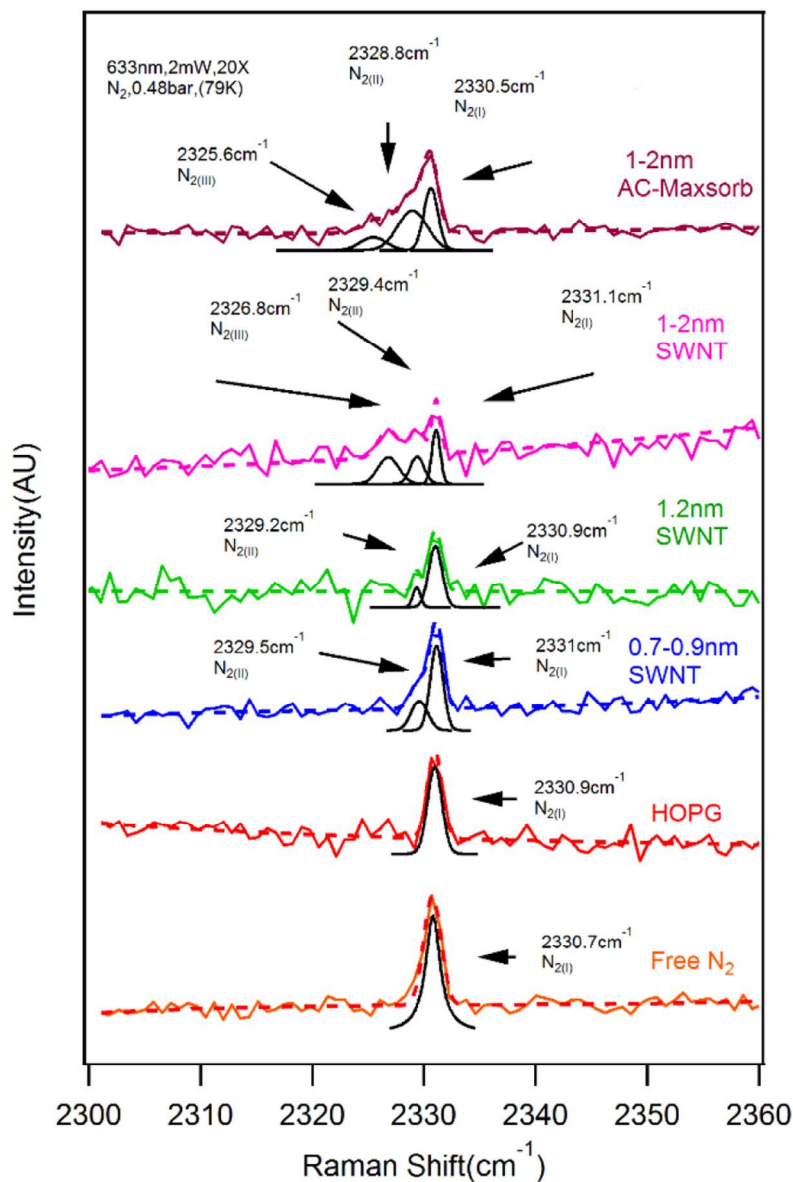
Figure 3: In situ N2 Raman adsorption at 79 K and 0.48 bar on various diameter SWNTs (as indicated), AC, and non-porous highly ordered pyrolytic graphite (HOPG), relative to free N2. The presence of a secondary N2(II) perturbation for the SWNT and AC but not HOPG is attributed to the formation of a multilayer adsorbed film associated with mesopore filling. A tertiary N2(III) mode in also visible in certain cases, as discussed in the main text. The dotted line shows the curve fitting and the solid black lines under each spectra shows the components of the fit.

84x118mm (300 x 300 DPI)
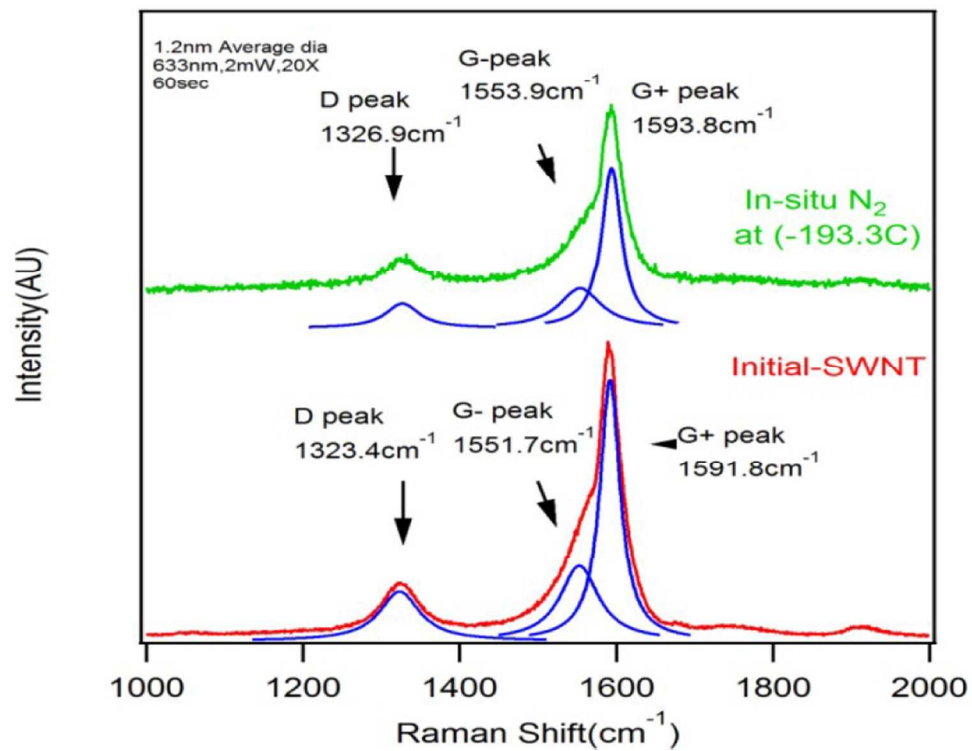
Figure 4: Carbon Raman modes show a shift in the D and and G peaks as a result of N2 adsorption at 79 K and 0.48 bar. Data for the 1.2 nm SWNT is shown

89x68mm (300 x 300 DPI)
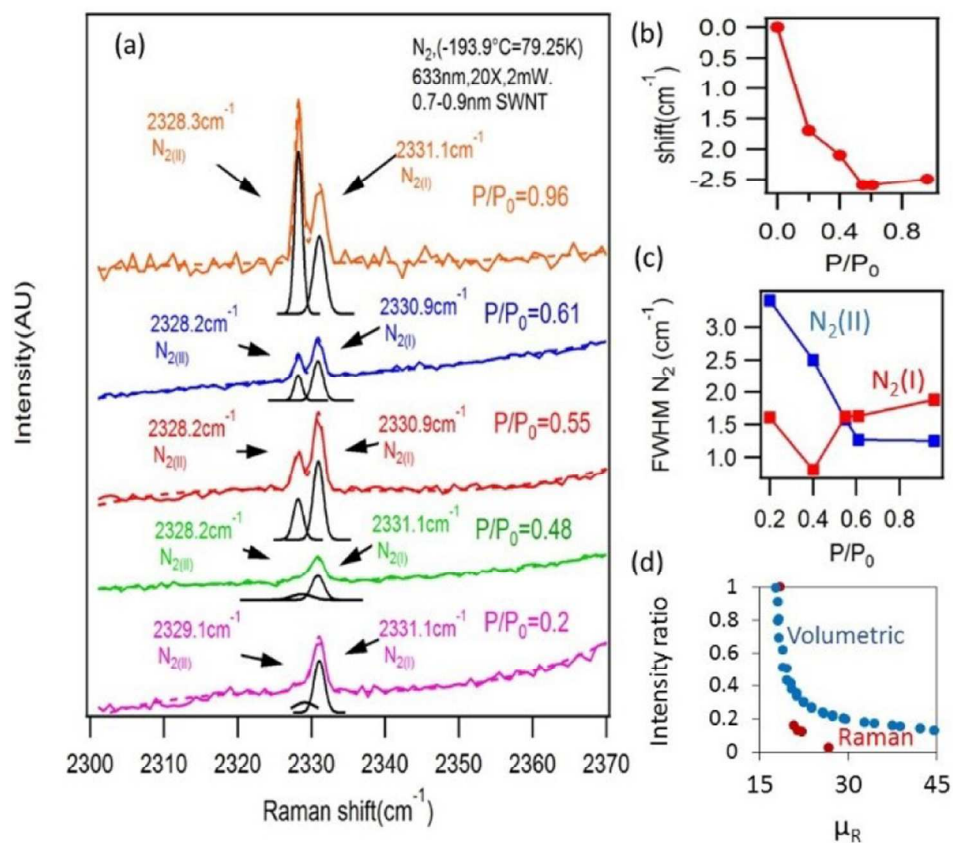
Figure 5: (a) In-situ Raman spectra of N2 adsorbed to the SWNT (0.7–0.9nm) at 79 K, as pressure is increased in the mesopore-filling regime. (b) Corresponding shift in peak position (N2(II)-N2(I)), (c) FWHM, and (d) relative Raman intensity plotted with the volumetric data. The Raman data in (b)–(d) are determined from Lorentzian fits from averages of multiple Raman spectra at multiple spots of the sample. See also Table S1 of the Supporting Information. In (d), both data sets have been normalized per the maximum value as P approaches Po.

84x74mm (300 x 300 DPI)
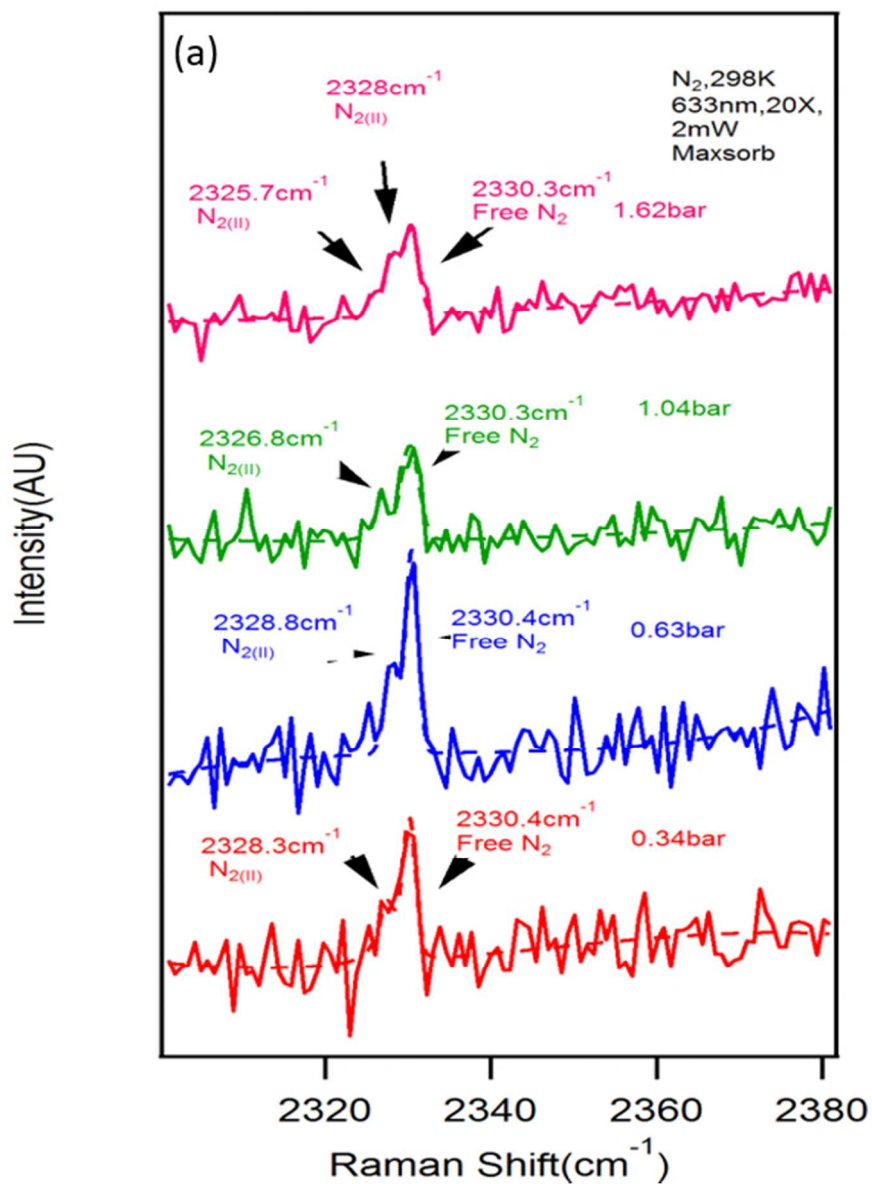
Figure 6: (a) In-situ N2 Raman spectroscopy of N2 adsorbed onto Maxsorb AC at room temperature as a function of pressure. (b) The intensity ratio of Raman at 298 K of the N2(II) to N2(I) Raman modes parallels the 77K volumetric data. In (b), the y-axis of both data sets is normalized to the value as P approaches Po.

165x215mm (96 x 96 DPI)
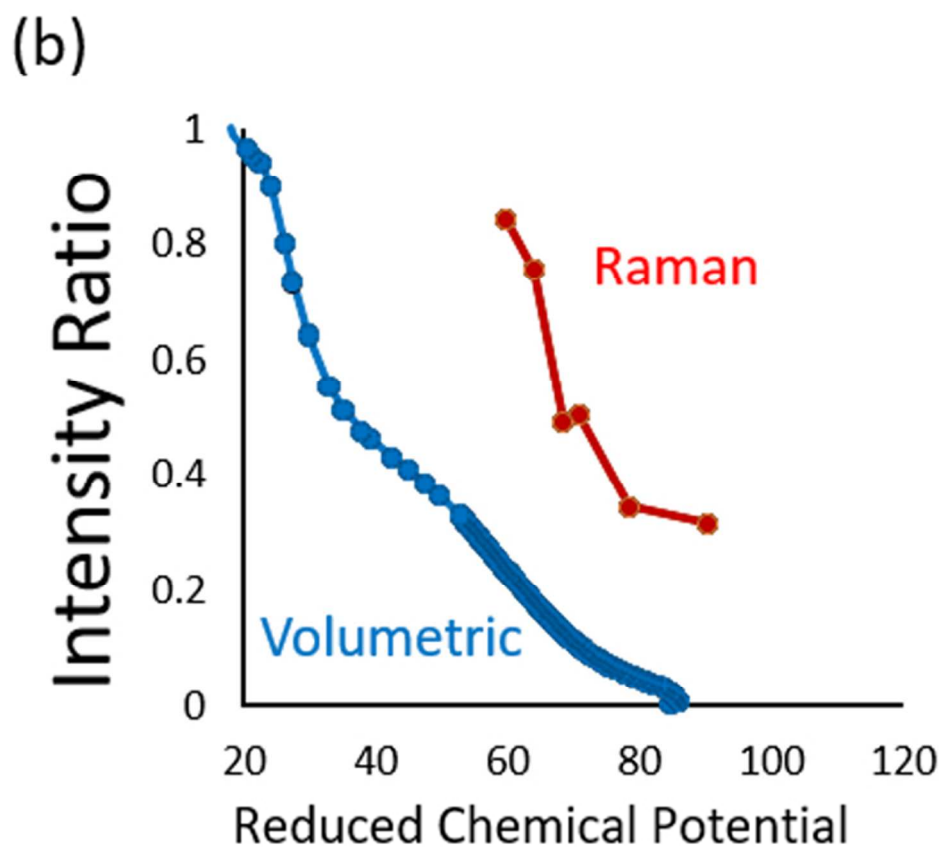
Figure 6: (a) In-situ N2 Raman spectroscopy of N2 adsorbed onto Maxsorb AC at room temperature as a function of pressure. (b) The intensity ratio of Raman at 298 K of the N2(II) to N2(I) Raman modes parallels the 77K volumetric data. In (b), the y-axis of both data sets is normalized to the value as P approaches Po.

174x160mm (96 x 96 DPI)
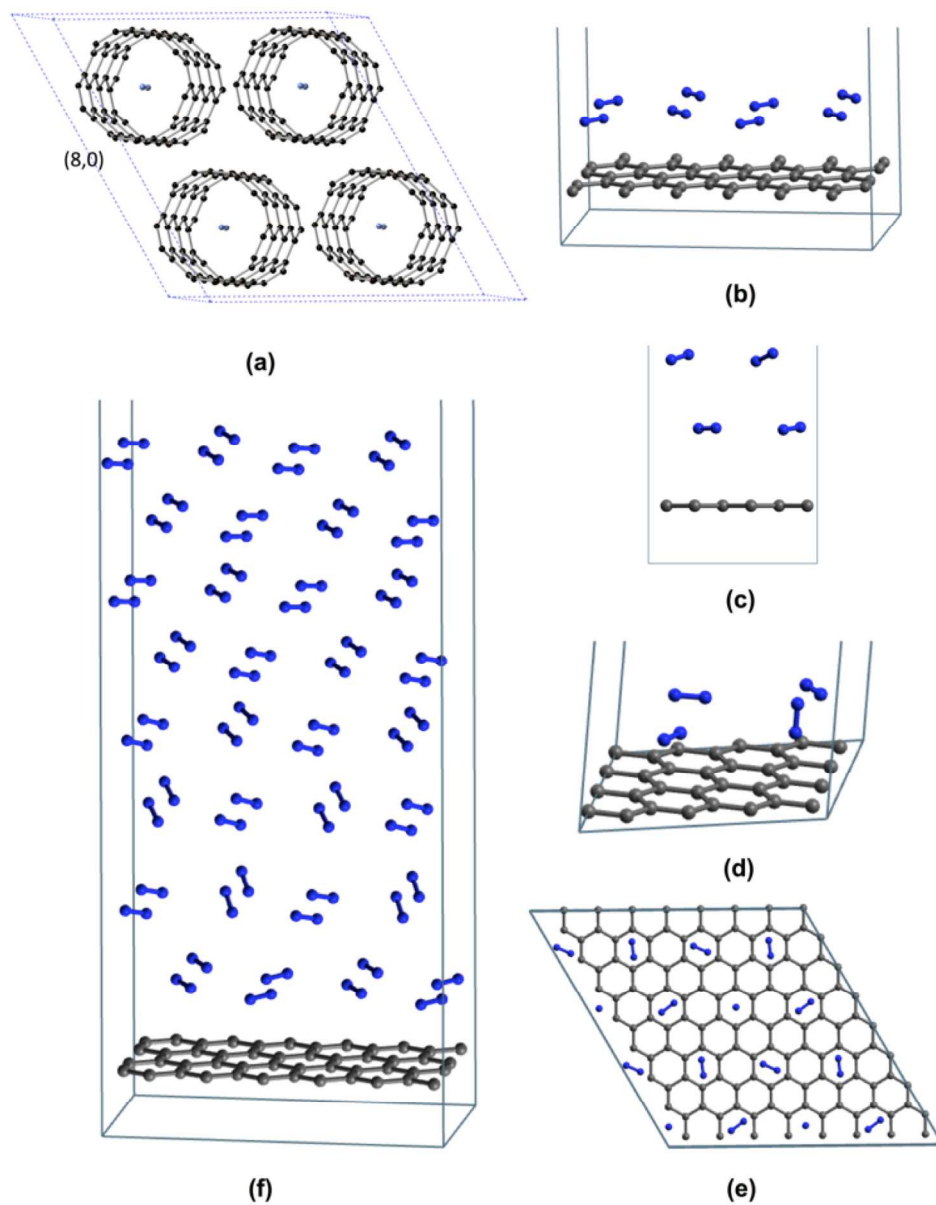
Relaxed structures for N2 thin films adsorbed on graphene. (a) Side view of monolayer herringbone. (b) Top view of bi-layer herringbone, the highlighted molecules are in the top layer (c) Side view of bi-layer herringbone. (d) side view and (e) top view of monolayer pinwheel (f, lower left) side view of an eight-layered N2 thin film relaxed from an initial herringbone configuration.

274x337mm (300 x 300 DPI)

84x47mm (300 x 300 DPI)